A NEW ELASTIC-VISCO-PLASTIC DAMAGE MODEL FOR ANNEALED ALUMINUM: THEORY, CALIBRATION AND VALIDATION

A. M. Habraken[1*], L. H. Zhang[1], X. C. Wang[2], S. Cescotto[1]

[1]Département MSM, Université de Liège, Chemin des Chevreuils, 1, 4000 Liège, Belgium
[2]First in MSM, now at Department of Mechanical Engineering, Division PMA, Katholieke Universiteit Leuven, Belgium

ABSTRACT

This article describes an energy based, two variables, isotropic damage model merged with Bodner's elasto-visco-plastic model and implemented in a non-linear finite element code. The procedure to identify the parameters of the model and its experimental validation are presented and applied to an annealed aluminum.

1. INTRODUCTION

The improvement of numerical simulations of industrial forming processes requires reliable constitutive models and rupture criteria. There are two common ways to predict rupture in the field of continuum mechanics [1]: classical behavior laws with a posteriori rupture criteria or continuum damage coupled constitutive laws. The first approach, easily implemented in any numerical code, is less general as it is difficult to find a single rupture criterion effective for all types of ruptures. This explains the tremendous amount of research work in continuum damage theory. Nowadays, elasto-plastic and elasto-visco-plastic continuum theories for isotropic damageable materials [2-5] are available and new extensions cover anisotropic cases [6,7].

Bodner & Partom [8] have proposed a unified theory for elasto-visco-plastic work hardening materials which has been widely used because of its ability to represent various material properties and to describe material response for steady or varying strain rate over a wide range of conditions [9]. Different extensions [10] have already been proposed to model kinematic hardening and damage evolution using one scalar damage variable.

In the present paper, Bodner's model is coupled with damage using two scalar variables in order to represent damage effects on both Young's modulus and Poisson's ratio. The true and effective strains and stresses are derived from elastic energy equivalence and respect the conservation of plastic dissipation rate. So, elastic, plastic and viscous material behaviors are affected by damage. Since, in Bodner's model, no yield surface is adopted, this feature is kept here: damage is not related to any threshold criterion but described by a continuous damage evolution law which takes into account a different damage behavior in tensile and compression states.

2. THE MODEL THEORY

2.1 Bodner's constitutive law

The general formulation of Bodner's model [8] is based on the additive decomposition of the total strain rate $\underline{\dot{\varepsilon}}$ into elastic $\underline{\dot{\varepsilon}}^e$ and inelastic $\underline{\dot{\varepsilon}}^p$ components which are both non-zero for all loading and unloading conditions :

$$\underline{\dot{\varepsilon}} = \underline{\dot{\varepsilon}}^e + \underline{\dot{\varepsilon}}^p \tag{1}$$

The elastic behavior follows Hooke's law, $\underline{\hat{\sigma}}$ is the deviatoric Cauchy stress and σ_m the mean stress. The superscript $\hat{}$ identifies a deviatoric tensor, the superscript ∇ the Jaumann rate and the subscript $_m$ the mean value of a tensor. G and χ are respectively the shear and bulk moduli, computed from Young's modulus E and Poisson's ratio ν.

$$\overset{\nabla}{\underline{\hat{\sigma}}} = 2G(\underline{\hat{\dot{\varepsilon}}} - \underline{\hat{\dot{\varepsilon}}}^p); \quad \dot{\sigma}_m = 3\chi\dot{\varepsilon}_m \tag{2}$$

The relation between $\underline{\hat{\sigma}}$ and $\underline{\dot{\varepsilon}}^p$ is:

$$\underline{\dot{\varepsilon}}^p = \frac{D_o}{\sqrt{J_2}} exp\left(-\frac{1}{2}\left(\frac{Z^2}{3J_2}\right)^n\right)\underline{\hat{\sigma}}$$

$$\text{with} \quad J_2 = \frac{1}{2}\underline{\hat{\sigma}} : \underline{\hat{\sigma}} \tag{3}$$

* Corresponding author : Tel: + 32 4 366 94 30; Fax: + 32 4 366 91 92;
Secretary: Tel: + 32 4 366 9248; Email : Anne.Habraken@ulg.ac.be

where Z is a total scalar hardening variable, composed of an isotropic part K and a directional part Z_D :

$$Z = K + Z_D \tag{4}$$

The directional component Z_D is computed by the projection of $\underline{\beta}$, a directional hardening symmetric tensor, on the direction $\underline{u}$ of the stress tensor :

$$Z_D = \underline{\beta} : \underline{u} \qquad \text{with } \underline{u} = \underline{\sigma} / \sqrt{\underline{\sigma} : \underline{\sigma}} \tag{5}$$

Both K and Z_D are assumed to occur under the action of two competitive mechanisms : strain induced hardening (first terms of equations 6 below) and temperature induced softening or recovery, represented by the second terms of equations 6:

$$\dot{K} = m_1 (K_1 - K) \dot{W}^p - A_1 K_1 \left(\frac{K - K_2}{K_1} \right)^{r_1} \tag{6.a}$$

$$\overset{\nabla}{\underline{\beta}} = m_2 (D_1 \underline{u} - \underline{\beta}) \dot{W}^p - A_2 K_1 \left(\frac{\sqrt{\underline{\beta} : \underline{\beta}}}{K_1} \right)^{r_1} \frac{\underline{\beta}}{\sqrt{\underline{\beta} : \underline{\beta}}}$$

$$\dot{\underline{\beta}} = \overset{\nabla}{\underline{\beta}} + (\underline{\Omega}.\underline{\beta} - \underline{\beta}.\underline{\Omega}) \tag{6.b}$$

where $\dot{W}^p$ is the rate of plastic work. The initial value of K at zero inelastic strain is K_0; K_1 is its maximum value; K_2 is its minimum (or stable) value at a given temperature at which creep is occurring. The initial and minimum (or stable) values of $\underline{\beta}$ are zero, which corresponds to an initially isotropic state. $\underline{\Omega}$ is the antisymmetric part of the velocity gradient tensor.

Bodner's model is totally defined by 14 parameters :

$$E, \nu, D_0, K_0, K_1, K_2, D_1, m_1, A_1, r_1, m_2, A_2, r_2, n$$

At room temperature, the terms related to the thermal recovery can be omitted and the number of parameters is reduced to 10. These are the material parameters to be determined.

2.2. Damage theory

Two scalar damage variables, called the deviatoric component d and the volumetric component δ, are used to represent the average material degradation due to microscopic defects [11]. As usual, true and effective stresses are related through the damage variables by:

$$\overline{\underline{\hat{\sigma}}} = \frac{\underline{\hat{\sigma}}}{(1-d)} \qquad \overline{\sigma}_m = \frac{\sigma_m}{(1-\delta)} \tag{7}$$

From the energy equivalence proposed by [12], the following relations are deduced for the elastic strains:

$$\overline{\underline{\hat{\varepsilon}}}^e = \underline{\hat{\varepsilon}}^e (1-d) \qquad \overline{\varepsilon}_m^e = \varepsilon_m^e (1-\delta) \tag{8}$$

Concerning plasticity, the plastic work rate $\dot{W}^p$ is conserved, this yields :

$$\overline{\underline{\dot{\varepsilon}}}^p = \underline{\dot{\varepsilon}}^p (1-d) \tag{9}$$

The damage evolution law comes from the one proposed by Lemaître [13]. It has been adapted to a multiaxial state and a two damage variable model :

$$\dot{d} = \frac{1}{2(1-d)} \left(\frac{< F(\underline{\sigma}) - \sigma_D >}{A(1-d)} \right)^s \dot{\varepsilon}_{eq}^r \tag{10}$$

with $<x> = x$ *if* $x > 0$ and $<x> = 0$ *if* $x \le 0$. σ_D, A, r, s are material constants. $F(\underline{\sigma})$ is a triaxiality function defined below which separates tensile, compression and shear stress states and introduces one new parameter α:

$$F(\underline{\sigma}) = (1-\alpha)\sqrt{3J_2} + 3\alpha\sigma_m \tag{11}$$

One should notice that the deviatoric damage d does not dependent on the shear component J_2 only, as the triaxiality function involves the mean stress σ_m.

The evolution of the volumetric damage variable δ is directly related to the evolution of d and assumes no volumetric damage increase in compression state :

$$\dot{\delta} = \tau \dot{d} \text{ if } \sigma_m > 0; \quad \dot{\delta} = 0 \text{ if } \sigma_m \le 0 \tag{12}$$

It has been checked experimentally that τ can be assumed constant in tensile state for common materials [14]. So, finally, damage is characterized by 6 parameters : $\sigma_D, A, r, s, \alpha, \tau$ This model allows to recover the well-known Kachanov creep law for $\tau = 1$, $s = \sigma_D = 0$.

2.3. Summary of the proposed model

According to damage theory, effective stresses and strains follow the classical behavior laws. So replacing $\underline{\sigma}$ by $\overline{\underline{\sigma}}$ and $\underline{\varepsilon}$ by $\overline{\underline{\varepsilon}}$ in Bodner's relations (1) to (6) and then using relations (7) to (9) between true and effective tensors, one can get the final equations :

$$\overset{\nabla}{\underline{\hat{\sigma}}} = 2G(1-d)^2 (\dot{\underline{\hat{\varepsilon}}} - \dot{\underline{\hat{\varepsilon}}}^p) - 4G(1-d)(\underline{\hat{\varepsilon}} - \underline{\hat{\varepsilon}}^p)\dot{d} \tag{13}$$

$$\dot{\sigma}_m = 3\chi(1-\delta)^2 \dot{\varepsilon}_m - 6\chi(1-\delta)\varepsilon_m \dot{\delta} \tag{14}$$

$$\dot{\underline{\hat{\varepsilon}}}^p = \frac{D_o}{\sqrt{J_2(1-d)}} \exp\left(-\frac{1}{2} \left(\frac{Z^2 (1-d)^2}{3J_2} \right)^n \right) \underline{\hat{\sigma}} \tag{15}$$

It is assumed that the Z hardening variable takes equal values in the actual damaged state and in the equivalent virgin state since its evolution is mainly controlled by the rate of plastic work which is the same in both states.

3.CALIBRATION METHOD

3.1 General principle

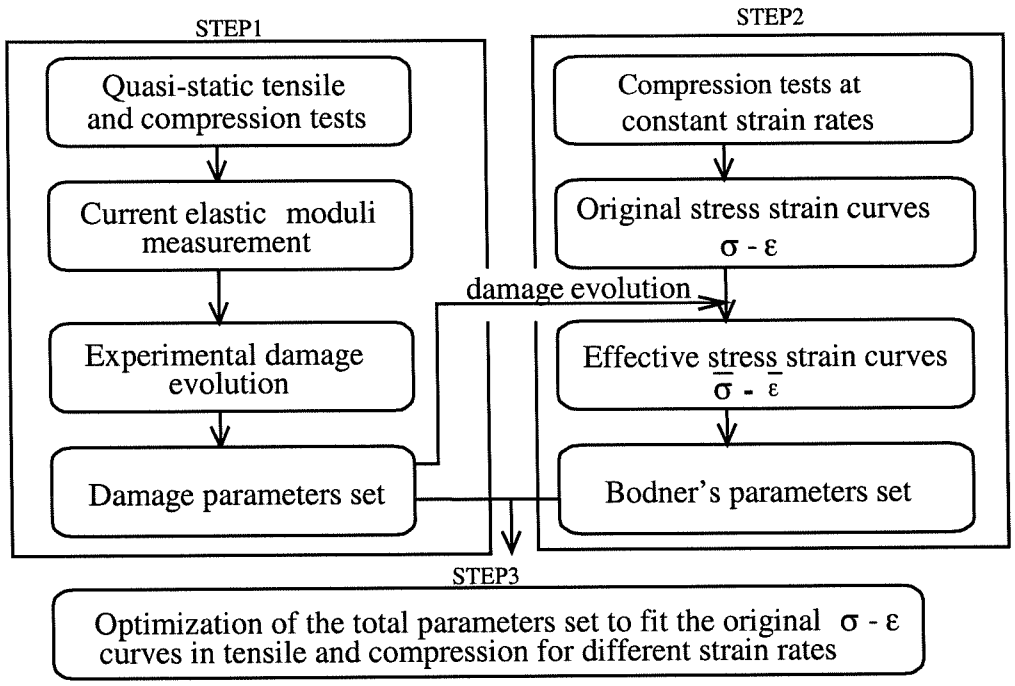

Figure. 1 Summary of parameter identification procedure for damage Bodner's model

The parameter identification procedure is summarized by figure 1. The parameters of the damage law and of Bodner's model (§2.1) applied to the effective behavior in the equivalent virgin state are first computed separately thanks to different experimental tests. Then the final set of parameters is obtained by an optimization process that modifies the less accurate parameters to reduce the difference between simulated and experimental values for uniaxial tests.

Each step of this parameter identification procedure is now described for the chosen annealed aluminum. This material is only available under the form of tubes of limited thickness.

3.2. Identification of damage parameters

3.2.1. Tensile tests

Cyclic loading-unloading quasi-static tensile tests performed on the whole tube allow to measure the evolution of $\overline{E}$ and $\overline{G}$. Figures 2a,b show the experimental results and two representative analytical curves which neglect or not the phenomena occurring at the beginning of plasticity. Both damage variables are directly deduced from these measures :

$$d = 1 - \sqrt{\frac{\overline{G}}{G_o}} \qquad \delta = 1 - \sqrt{\frac{\overline{\chi}}{\chi_o}} \tag{16}$$

where $\overline{\chi}$ is the bulk modulus computed by :

$$\overline{\chi} = \frac{\overline{E}.\overline{G}}{3(3\overline{G} - \overline{E})} \tag{17}$$

Figures 3a and b show the experimental damage evolutions as well as reduced curves used further as explained in section 3.2.3.

According to the classical macroscopic damage theory [4], extrapolated value of Young's and shear moduli $E_o^{(1)}, G_o^{(1)}$ should be used. This gives damage values growing in a monotonic way from zero as represented by model 1 curves on figures 3a and b. The difference between the elastic moduli $E_o^{(2)}, G_o^{(2)}$ and

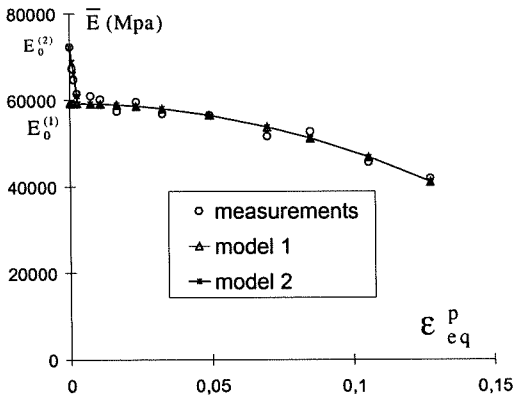

Figure 2.a Young's modulus from tensile tests.

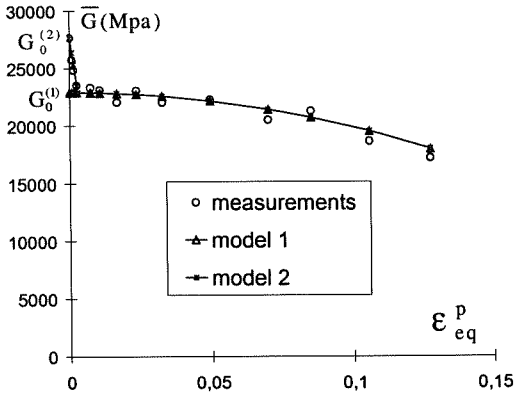

Figure 2.b Shear modulus from tensile tests.

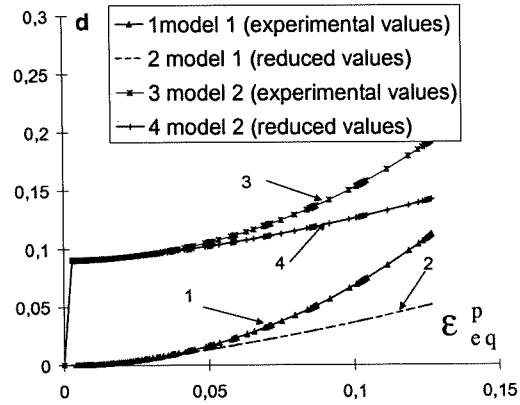

Figure 3.a Deviatoric damage from tensile tests.

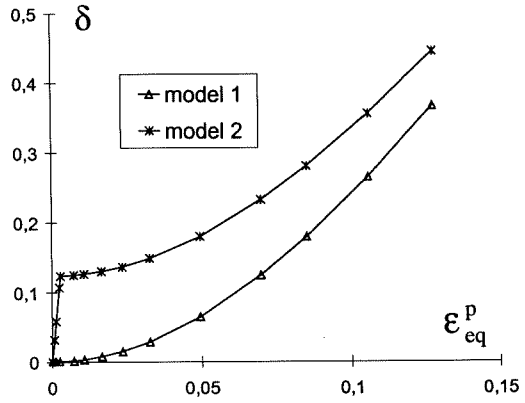

Figure 3.b Volumetric damage from tensile tests.

their extrapolated value $E_o^{(1)}, G_o^{(1)}$ is assumed to be related to plasticity entrance and not to damage [15].

However [2,16], this fact could also be linked to a nucleation void rate increasing the void volume fraction very quickly at the plasticity entrance and followed by a smoother void growth rate

In the present aluminum 2024, optic microscopy has demonstrated the presence of precipitates which exhibit a matrix decohesion after plasticity entrance. Such a phenomenon is not seldom. For instance in Pardoen's thesis [17] dedicated to copper, an initial void volume fraction is assumed to take into account the precipitate decohesion appearing under microscopic strains.

Here, the two assumptions are considered: damage is computed according to $E_o^{(1)}, G_o^{(1)}$ or $E_o^{(2)}, G_o^{(2)}$. This yields to check two models : Model 1 where damage evolution is defined according to. (10) and (12) and Model 2 where damage follows a quick linear increase at plasticity entrance and, afterwards is modeled by. (10) and (12).

The constant damage ratio $\tau = \delta / d$ assumption is reasonably checked . Its variation is in the range [3.24, 4.12] for Model 1 and [1.37, 2.30] for Model 2.

3.2.2 Compression tests

Cyclic loading-unloading tests were performed on small cylinders (diameter 7 mm, height 7 mm) and the evolution of Young's modulus is shown on figure 4.a

To reach the damage parameters in compression thanks to relations (16) and (17), measurements of the effective shear modulus should be available. Practical experimental problems prevent us to accurately measure this modulus. Adding the assumption of no volumetric damage in compression (equation 12) yields the following relation :

$$d = 1-(1-D)\sqrt{\frac{E_o}{3G_o - 3G_o(1-D)^2 + E_o(1-D)^2}}$$

with $D = 1-\sqrt{\frac{\bar{E}}{E_o}}$ (18)

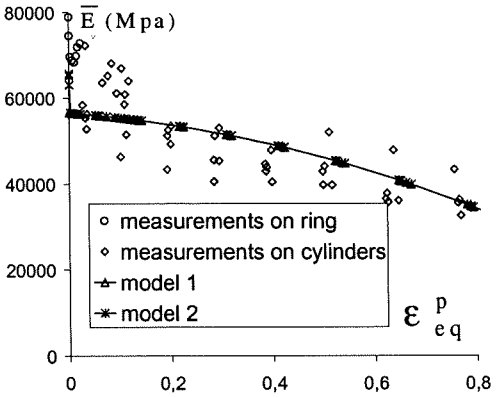

Figure 4.a Young's modulus from compression tests.

So, the experimental evolution of deviatoric damage (figure 4.b) is deduced from figure 4a and relation (18).

3.2.3 Identification of damage parameters

Let σ be the true value of the stress in uniaxial tests. The triaxiality function (11) is straightforward :

$$F(\underline{\sigma}) = (1-2\alpha)^{\theta}\sigma \qquad (19)$$

with θ=0 in tension and 1 in compression.

The integration of the damage evolution law defined by (10) results in the following relation for model 1 :

$$d = 1-(1-\frac{(S+2)(1-2\alpha)^{\theta s}}{2A^S}\int_o^{\varepsilon^p_{eq}}\sigma^s d\varepsilon^p_{eq})^{1/S+2} \qquad (20)$$

if, from the beginning, we assume that there is no effect of strain rate on damage evolution (r=1) and no threshold value (σ_D=0). These additional assumptions are related to the experimental damage observations (figures 3a and 4b) and to the low viscosity effect observed in section 3.3.2 for this aluminum.

For model 2, the principle is identical except that the damage evolution law is first linear until damage has reached a transition value.

The problem is now reduced to a classical inverse method: knowing relation (20) and experimental curves (figures 3a and 4b), let us find the best set of parameters (S, α, A) that minimizes the differences between model and experiments. In fact for tensile state, the reduced values (figure 3a) and not the experimental ones have been used as a target value. This is justified by the fact that the plastic strain reached during tensile tests is much smaller than in compression. Furthermore, the range covered by tensile tests (figure 3a) corresponds to the region of maximum scatter of the compression results (figure 4a). This choice allows to reach an effective

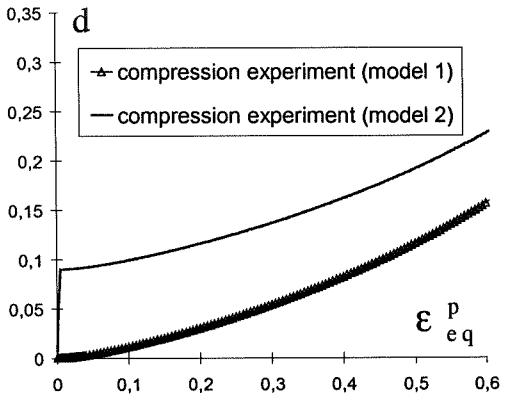

Figure 4.b Deviatoric damage from compression tests.

reference curve $\bar{\sigma}_{eq}\bar{\varepsilon}_{eq}$ compatible with both tensile and compression experimental curves

Table 1 summarizes the final damage parameters provided by the inverse method.

	Model 1	Model 2
S	2,006	2,5274
A (Mpa)	256.74	250
σ_D (Mpa)	0	0
r	1	1
α	0.216	0.2136
d_1 (model 2)	0	0,09
ε_{eq1} (model 2)	0	0,0029

Table 1 Parameters for damage models 1 and 2

3.3. Identification of Bodner's parameters

3.3.1.Compressions at various strain rates

Compression tests on cylindrical samples have been performed for various constant strain rates at room temperature. For a strain rate of 20 s^{-1}, a temperature increase of ≈ 80°C can be reached during a compression test up to 70% strain. The temperature dependence of the material behavior has been checked by quasi-static uniaxial compression tests at room temperature (16,5°C) and at 100°C. Using these results, a quasi-adiabatic assumption (for tests performed at $\dot{\varepsilon}$ = 10 s^{-1} and 20 s^{-1}) and the damage evolution law (Model 1) defined in the

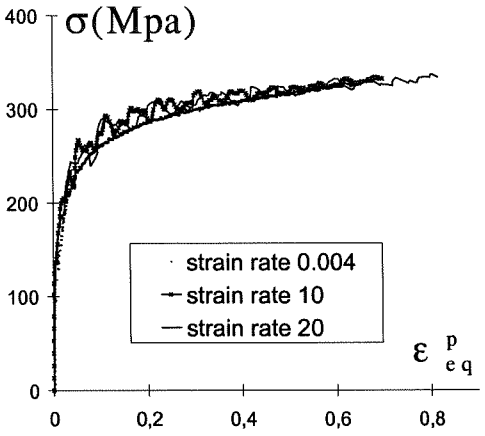

Figure 6a. Compression at different strain rates. Experimental results.

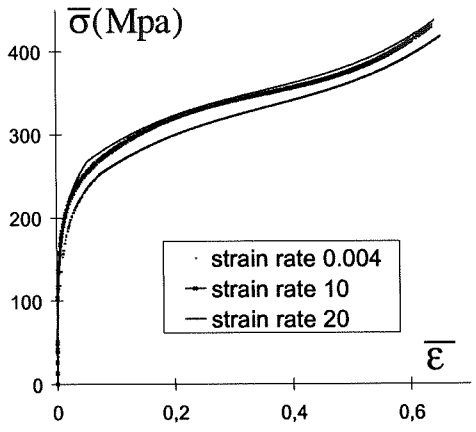

Figure 6b. Compression at different strain rates. Effective stress strain curves.

preceding sections, the effective stress strain curves (figure 6b) can be deduced from the experiments (figure 6a). It is seen that the viscous effect on this material is limited for the considered strain rates.

3.3.2 Identification of Bodner's parameters

The procedure applied to identify Bodner's parameters comes from [18]. Bodner's law for a uniaxial test is expressed the by following relation :

$$\frac{\sigma}{Z} = \left[2 ln\left(\frac{2D_o\sigma}{\sqrt{3}\dot{\varepsilon}^p|\sigma|} \right) \right]^{-1/2n} = f \qquad (21)$$

where $\dot{\varepsilon}^p$ is constant for the selected tests. As D_o, is chosen by the model user, the constant f is easily computed for each experiment once n is known. At room temperature, thermal softening effect is negligible. So, the isotropic and directional hardening laws reduce to their first term in (6). For uniaxial tests, one gets:

$$\dot{K} = m_1(K_1 - K)\dot{W}^p \quad \text{with} \quad K(0) = K_o \qquad (22)$$

$$\dot{Z}_D = m_2(D_1 - Z_D)\dot{W}^p \quad \text{with} \quad D(0) = 0 \qquad (23)$$

$$Z = K + Z_D \qquad (24)$$

The derivative of the axial stress with respect to plastic work is then used to find m_1 and m_2 .From (21) to (24) one gets:

$$\gamma(\sigma) = \frac{d\sigma}{dW^p} = f(m_1(K_1 - K) + m_2(D_1 - Z_D)) \qquad (25)$$

Theoretically, this function should allow to define two linear parts represented on figure 7, which also defines the saturation stress σ_s and the coefficient a.

- for small plastic strains, isotropic hardening is equal to K_o while directional hardening is increasing :

$$K = K_o \qquad Z_D = Z - K_o = \frac{\sigma}{f} - K_o \qquad (26)$$

- for large plastic strains, directional hardening has reached its saturation level D_1 while isotropic hardening is increasing :

$$Z_D = D_1 \qquad K = Z - D_1 = \frac{\sigma}{f} - D_1 \qquad (27)$$

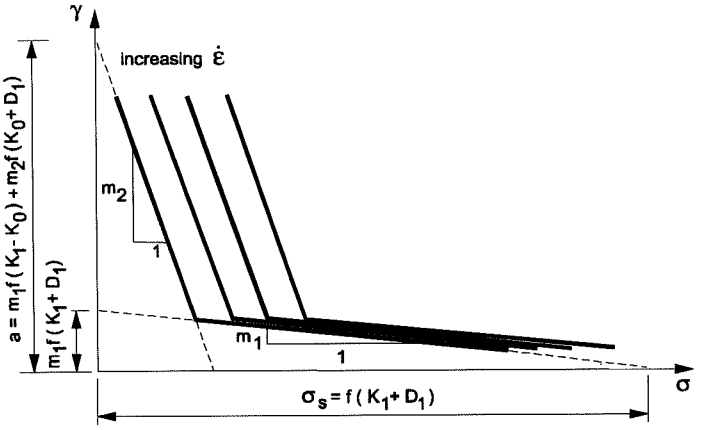

Figure 7. Function $\gamma(\sigma)$ for an ideal theoretical case.

However, the function γ issued from the effective stress strain curves (figure 6b) is quite far from this theoretical shape, which leaves quite a large range to chose m_1 and m_2.

The value of the saturation stress σ_s can be used to find the strain rate sensitivity coefficient n. Combining relation (21) and the definition of σ_s (figure 7), gives :

$$ln\,\sigma_s = -\frac{1}{2n} ln(2\,ln\frac{2D_o}{\sqrt{3}\dot{\varepsilon}^p}) + ln(K_1 + D_1) \qquad (28)$$

Again, the tests do not yield to co-linear points, which leaves some freedom to define the value of n. The hardening values are extracted from the stress strain curves, relation (21) and from the value of f:

$$\sigma_o = fK_o;\ D_1 = \frac{\sigma_1}{f} - K_o;\ K_1 = \frac{\sigma_s}{f} - D_1 \quad (29)$$

where σ_o is the yield stress, σ_1 the stress at saturation of directional hardening and σ_s the stress saturation value.

The preceding procedure helps to define the range of the different parameters. The final set of parameters is then produced by optimization

3.4 Set of parameters

	Damage Model 1	Damage Model 2
Parameter	Values	Value set
E (Mpa)	72250	65660
ν	0,31	0.31
D_o (s^{-1})	10^8	10^8
K_o (Mpa)	106.584	99.506
K_1 (Mpa)	341.744	358.661
K_2 (Mpa)	106.584	99.506
D_1 (Mpa)	231.445	239.131
m_1	0.091	0.0125
m_2	0.33	0.43
n	5.5126	6.8524

Table 2. Bodner's parameters to recover the effective stress strain curves (Models 1 and 2)

At this level, tables 1 and 2 define the whole set of parameters set for Models 1 and 2. One can check that simulated curves are close to the experimental ones (figures 8a,b). The RR' line defines the experimental rupture in tensile state.

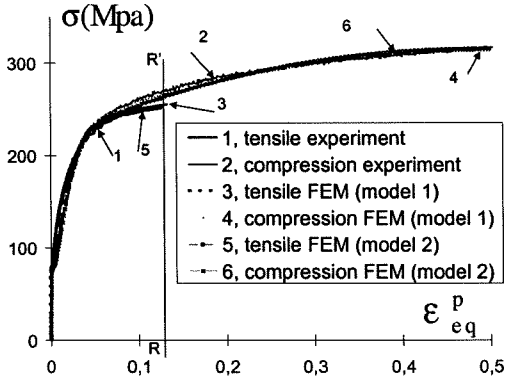

Figure 8.a. Stress-strain curves.

4. VALIDATION

4.1. Introduction

In this section, experiments and simulations are performed in order to check the ability of the model to predict fracture initiation and development as well as the global response of the tested structure. To achieve this, the damage evolution rule should be accurate enough to follow the different steps of void nucleation, growth and coalescence and other mechanisms of a ductile fracture. As the model is macroscopic and not dedicated only to one rupture type, one cannot expect perfect agreement with the experiments but a general information should be given by the simulations.

Since damage coupled constitutive models are softening ones, strain localization appears, governing equations lose their ellipticity and a pathological mesh dependency of the solution is pointed out for classical damage elasto-plastic laws.

Various solutions have been proposed to overcome this difficulty : non local approach [19], Cosserat theory [20] viscous regularization [21], gradient plasticity [22]... In the present research, although the material viscosity is low, it seems to be sufficient to prevent mesh dependence. This is examined in section 4.2.

Another key point is the rupture criterion to detect fracture initiation and development. The experiments were filmed with a classical camera which allows to roughly detect the macrocrack appearance and its evolution. Comparisons of the simulation results and the experiments show that damage is correctly localized as well as its propagation. The analysis of the results demonstrates that a simple deviatoric damage threshold value is not very accurate to detect rupture but can be used. Finally, the experimental fracture always happens simultaneously with a strong drop in the global force-displacement or force-time curve.

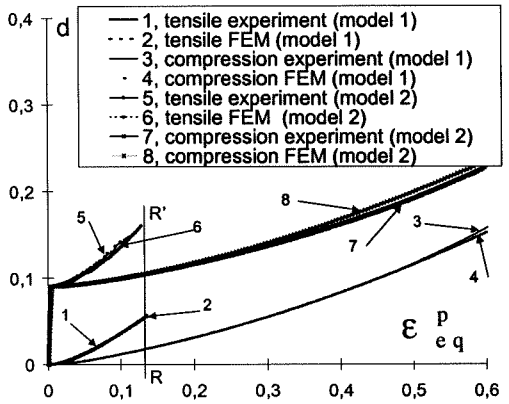

Figure 8.b. Deviatoric damage versus strain.

In our simulations, the damage variables d and δ are not numerically limited, they increase according to their evolution rule up to one. This means that even after micro-crack initiation, which is not accurately defined with this macroscopic model, the element stiffness and stresses are still non zero but strongly reduced.

For a localized zone with very high damage or a larger zone with medium damage, the stiffness decrease yields to an effective drop in the global force response. This could represent numerically well the final fracture. However in some cases, convergence problems appear and prevent to go on with the simulation until a significant drop of the curve is noticeable. This generally happens when the maximum of the curve is already passed over and some material points have already reached high damage value. So, one can predict that global rupture will happen soon but the computation does not go on until this point. As checked for the notch test, the final global force displacement curve decrease is strongly mesh dependent, so the model is not able to accurately detect the final fracture.

Finally, this validation part also allows a comparison of the constitutive law efficiency according to the chosen damage evolution model (Models 1 or 2, see section III.2.1 of Part 1).

All the simulations are performed with the nonlinear finite element code LAGAMINE developed in the MSM Department. The 2D and 3D finite elements are of mixed type [23,24]

4.2.. Mesh dependence

The geometrical details of the axisymmetric test specimen are given on figure 9. The test is driven by the displacement of one extremity at the constant velocity of 0,005 mm/s while the elongation of the middle part is measured between points AA'.

Six different meshes have been used to check the stability of the simulation results. They differ by the mesh density at the notch level. Figure 10 shows the finest and the coarsest meshes

These meshes are characterized by the ratio b between the diagonal of the smallest element and the notch radius. It ranges from b=1% to b=10.4%. The simulation results (using Model 1) are summarized on figures 11 and 12.

From figure 11, it is clearly seen that the mesh dependence only appears after necking.

Figure 12 shows a small variation of deviatoric damage with the mesh except for the center point and the coarsest mesh.

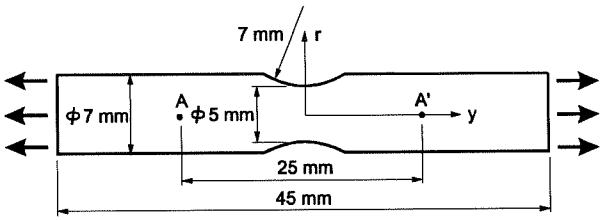

Figure 9. Sample description – Notch test

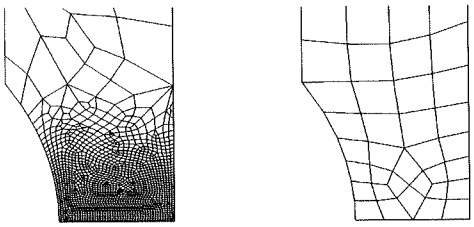

Figure 10. Finest and coarsest meshes for notch test

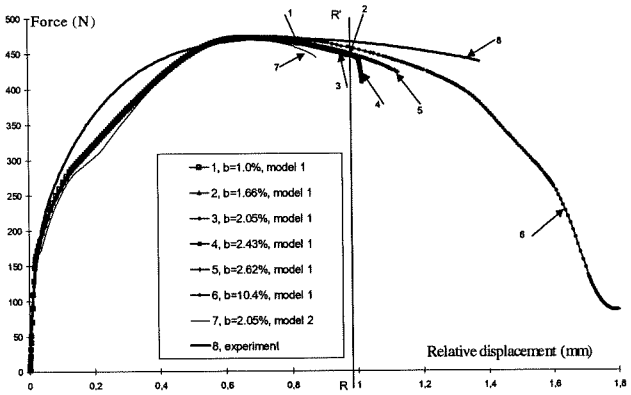

Figure 11. Experimental and simulated force-displacement curves for different meshes.

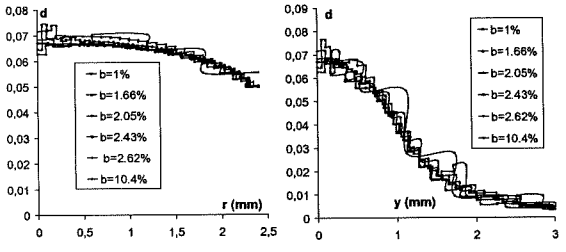

Figure 12. Deviatoric damage along the radius r and the axis y of the specimen for an elongation of 0.65 mm

However, if some smoothing procedure is used to represent the map of deviatoric damage, one will find that the level and the size of the localized damage zone is quite identical for each mesh, even the coarsest one.

Since this notch test is the only validation test for which necking appears, it can be assumed that mesh dependency will not significantly affect the validation procedure.

4.3. The notch test.

The tensile test has a large notch radius (figure 9) which means that damage is maximum at the center of the neck, leading to a well-known cup-cone fracture [25]. For this test, the stress field is characterized by a very high triaxiality index: $J_2/\sigma_m \cong 1.4$ instead of 0.57 for a uniaxial tensile test.

The simulation results considered hereafter were obtained with a fine mesh (b=2.43%). Figures 13a,b show maps of the triaxiality index, and of the deviatoric damage obtained with Model 1 at the moment identified as the "experimental rupture" (line RR' in figure 11). Model 2 gives the same distribution for these variables; a difference exists only on their values. For this reason, we will not show such figures for model 2, neither for this example nor for the following ones.

4.4. Tensile test on a perforated specimen

The sample geometry is shown on figure 14. It is cut from the tube wall. A gauge length AA' of 10 mm is used for regulation: the end displacements are controlled so that a relative constant velocity of 0.01 mm/sec between A and A' is maintained. The specimen is discretized by 8-node 3D mixed finite elements. The ratio b between the diagonal of the smallest element and the radius of the hole is 9%. The ratio c between the maximal side and the minimal side of the smallest element is 2.3.

The experimental and computed force-displacement curves are given on figure 15.a. Generally speaking, Model 2 is closer to the first test in which fracture takes place earlier, while Model 1 is closer to the second test in which fracture happens later. The calculated force–time curves capture very well the drop of the experimental curve both for Models 1 and 2. But for the force-displacement curves, only Model 2 follows this sudden drop while Model 1 shows only a little decrease of the force. This is due to a quick elongation developed at the moment of fracture.

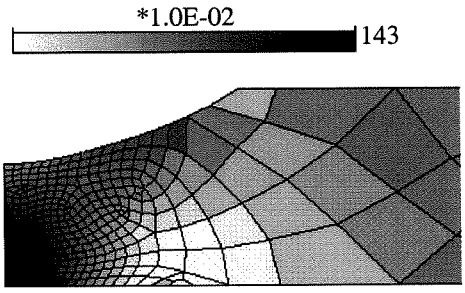

Figure 13.a.Triaxiality index at the moment of experimental rupture

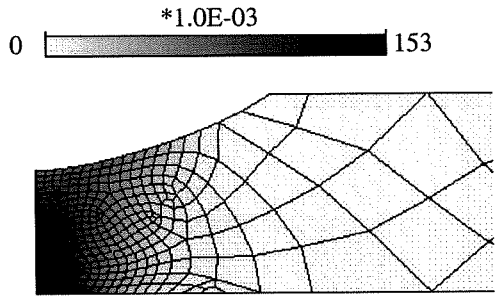

Figure 13.b.Deviatoric damage at the moment of experimental rupture

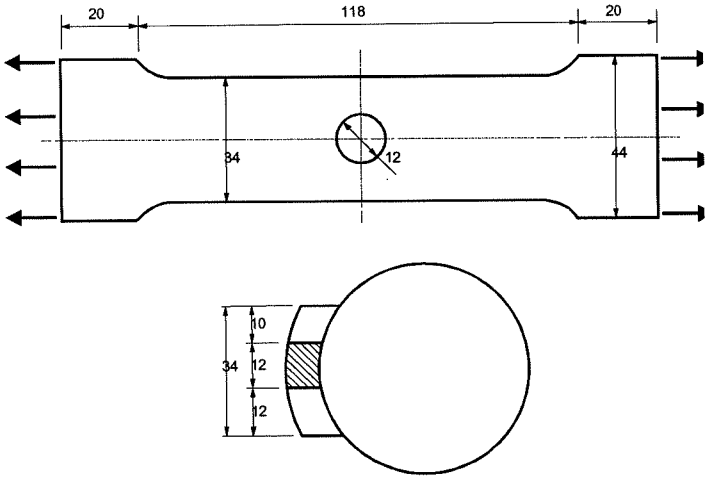

Figure 14. Tensile test on a perforated specimen: geometry

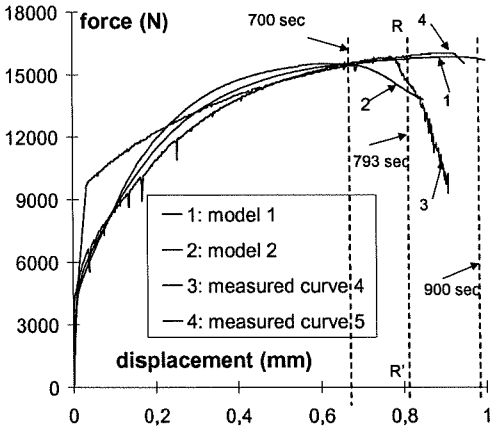

Figure 15.a. Tensile test of perforated specimen
Tensile force versus relative displacement of base AA')

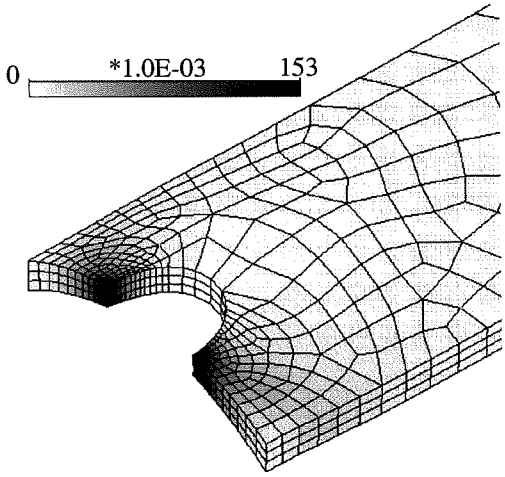

Figure 15.b. Tensile test of perforated specimen
Deviatoric damage at the moment of rupture RR'

Figure 15.b shows the distribution of deviatoric damage for Model 1 at the moment of rupture (RR'). The maximum deviatoric damage, d_{max} reaches 0.15 and all values of d greater then 0.14 are located within 1.2 mm from the hole root.

4.4. Bending test

The third example is a three points bending test on the notched whole tube is loaded (figure. 16).

The tube is discretized in 8-node 3D mixed finite elements. The b ratio is about 12% and the c ratio is 9.5 for a first mesh with one layer of elements through the thickness. This relatively high c ratio leads to poorly shaped elements near the notch root. So, a second mesh with two layers of elements through the tube thickness was used. Its c ratio is 4.75.

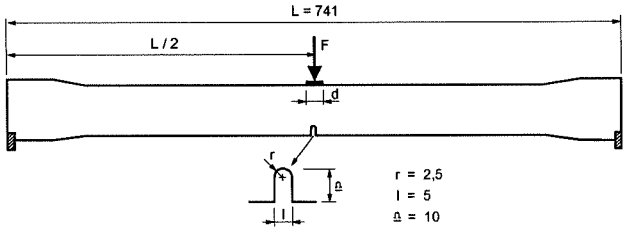

Figure 16. Three point bending test: geometry

The experimental and computed force-displacement curves are given on figure 17. From the experiments, it has been checked that local fracture appears earlier than the final rupture due to the high strength of the tube section. This fact explains why the experimental local rupture indicated by RR' seems far away from the actual

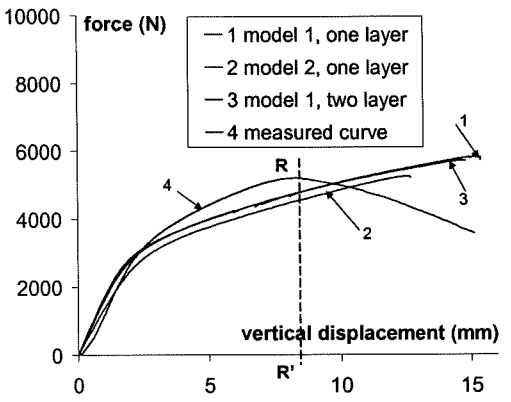

Figure 17. . Three point bending test.
Force displacement curves.

fracture of the structure.

From the distribution of deviatoric damage (not shown for brevity) obtained with the second mesh, one can realize that damage is highly concentrated and cannot be represented with a coarse mesh. To simulate the high damage gradient, the b and c ratios should be even smaller than the smallest ones (b=12%, c=4.75). A strong damage variation between the internal and external layers proves the necessity of a very low c ratio.

4.4. Shear test on perforated tube

The shear dominated test is shown on figure 18. For simulating this test, a coarse (b=50%, c=2.5) and a fine (b=15%, c=4.1) meshes are used. As could be expected, the first mesh gives poor results with a lot of strain or damage discontinuities. The second one is reasonable.

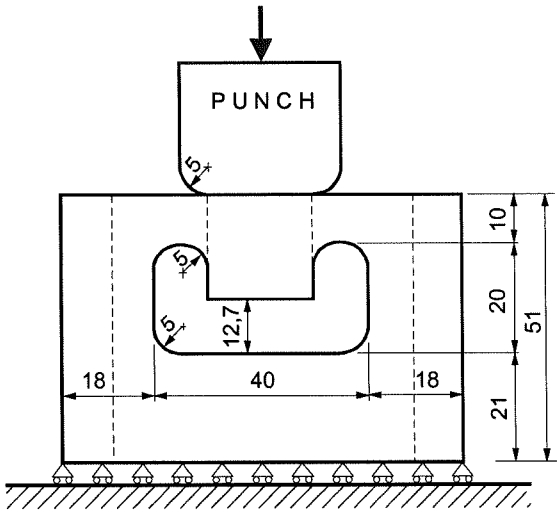

Figure 18a: Shear test: geometry and loading (side view)

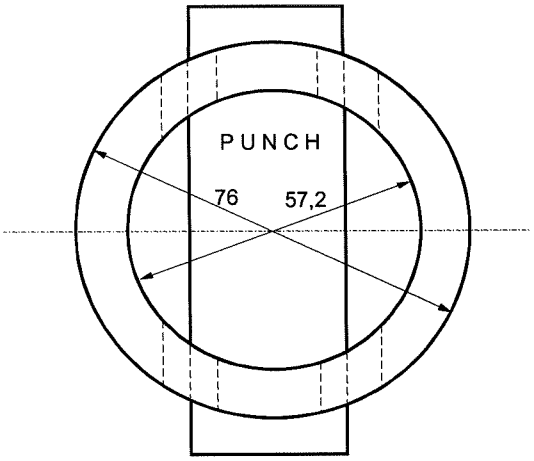

Figure 18b: Shear test: geometry and loading (top view)

Figure 19.a shows force-displacement curves. The drop of the simulated curves occurs later than in the experiments except with Model 2, mesh 2. Figure 19.b shows the deviatoric damage d at experimental rupture (line RR', figure 11.b) for mesh 2. It can be seen that the global simulation results (force-displacement curve) are not affected by the discretization, except for the curve drop. With both meshes, both damage models predict the maximum deviatoric damage and the maximum equivalent strain at the location of the experimental fracture (internal face, above the notch). No matter the chosen damage model, the finer mesh simulates more accurately the damage or strain gradients: higher maxima are reached and they are more localized. The distribution of shear stress has a maximum above the hole; however local hydrostatic stress concentration induces a strong gradient of the triaxiality factor.

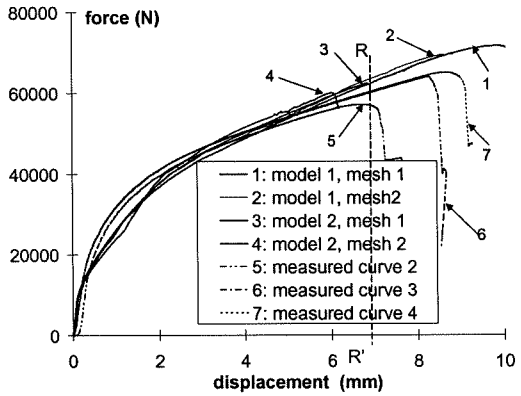

Figure 19.a. Shear test: force displacement curves.

5. CONCLUSION

An extension of Bodner's model to include damage has been proposed. Two damage evolution models have been considered. They differ by the way the initial drop of Young's modulus for small plastic strain is taken into account The calibration procedure is well developed and, despite some experimental inaccuracies and difficulties due to the fact that the material tested was only available under the form of tubes, it has successfully been applied on the considered aluminum.

The model and the calibrated material parameters allow to represent the material behavior from a macroscopic point of view. Both proposed damage evolutions have been checked for various loading states and, globally speaking, they efficiently predict rupture.

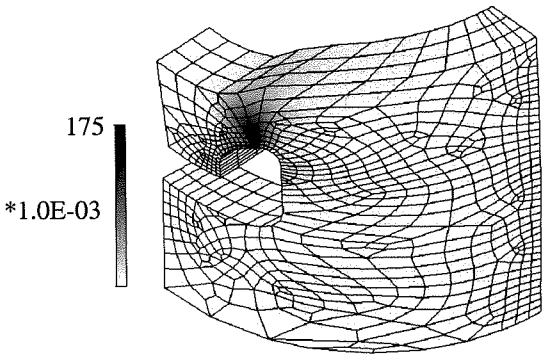

Figure 19.b. Shear test: deviatoric damage at the moment of rupture RR'

Acknowledgement A.M. HABRAKEN wishes to thank the FNRS (Belgian National Scientific Research Fund) as well as the Région Wallonne for the financial support of her work.

References

1. Zhu Y.Y., Cescotto S. and Habraken A.M. (1992) A fully coupled elastoplastic damage modeling and fracture criteria in metalforming processes, *J. of Mater. Processing Technology* **32**, 197-204.
2. Gurson A.L. (1977) Continuum theory of ductile rupture by void nucleation and growth. *J. Engng. Materials Technology* **99**, 2-15.
3. Tvergaard V. (1982) Material failure by void coalescence in localized shear bands, *Int. J. Solids & Struct.* **18**, 659-672.
4. Lemaître J., Chaboche J.L. (1985) *Mécanique des matériaux solides*, Dunod, Paris.
5. Perzyna P. (1986) Internal state variable description of dynamic fracture of ductile solids, *Int. J. Solids & Struct.*, **22**, 797-818.
6. Benzerga A., Besson J., Pineau A. (1997) Modèle couplé du comportement-endommagement ductile de tôles anisotropes. *3ème colloque national en calcul des structures*, 20-23 mai, Giens, France.
7. Habraken A.M., Charles J.F., Cescotto S. (1997) Calibration and validation of an anisotropic elasto-plastic damage model for sheet metal forming, in *Damage Mechanics*, in *Engineering Materials*, Ed. G.Z. Voyiadjis, J.W. Ju, J.L. Chaboche, **46** *Studies in Applied Mechanics*, Elsevier, 401-420.
8. Bodner S.R. ,Partom Y. (1975) Constitutive equations for elastic-viscoplastic strain-hardening material, *J. of Applied Mechanics*, **42**, 385-389.
9. Zhu Y.Y. and Cescotto S. (1994) A unified elasto-visco plastic theory of the Bodner model and an effective integration procedure, *J. DYMAT* **1**, 63-99.
10. Bodner S.R. (1985) Evolution equations anisotropic hardening and damage elastic-viscoplastic materials, *Plastic today*, ed. A. Saczak & G.Biandsi, Elsevier, 471-482.
11. Ladevèze P. (1984) Sur une théorie de l'endommagement anisotrope, Rapport interne 34, LMT, Cachan, France.
12. Cordebois, J.P., Sidoroff, F.(1979), Damage induced elastic anisotropy, F. *Euromech*, **115**.
13. Lemaître, J. (1985) Coupled elastoplasticity and damage constitutive equations, *J. Comp. Meth. in Appl. Mech. and Eng.* **51**, 31-49.
14. Gattoufi, B. (1984) Effets de la prédéformation due au filage sur le comportement des métaux, Thèse de docteur de 3ème cycle, Université de Paris.
15. Chevalier, L. Etude des caractéristiques des matériaux tréfilés après l'opération de tréfilage, Thèse de doctorat, Université de Paris 6, ENS Cachan, 1988.
16. Leblond, J.B., Perrin, G., Devaux, J. (1995) An improved Gurson-type model for hardenable ductile metals, *Eur. J. Mech. A/Solids*, **14**, 499-527.
17. Pardoen, T. (1998) Ductile fracture of cold-drawn copper bars : experimental investigation and micromechanical modeling, Doctorat en sciences appliquées, Université de Louvain-La-Neuve.
18. Chan, K.S., Bodner, S.R., Lindholm, U.S. (1988) Phenomenological modeling of hardening and thermal recovery in metals, *J. of Eng. Mat. & Techn.*, **110**, 1-8.
19. Bazant, Z.P. ,Chang, T.P. (1984) Instability of non-local continuum and strain averaging, ASCE, *Jnl. of Eng. Mech.*, vol. 110, **10**, pp. 1441-1450.
20. De Borst, R. (1991) Simulation of strain localization: a reappraisal of the Cosserat continuum, *Engineering Computations*, **8**, 317-332.
21. Loret, B., Prevost, H. (1990) Dynamic strain localization in elasto-(visco)-plastic solids : Part 1 General formulation and one-dimensional examples, *Comp. Meth. in Appl. Mech. Eng.*, **83**, 247-273.
22. Li, X.K., Cescotto, S. (1995) Finite element method for gradient plasticity at large strains, *Int. J. Num. Meth. in Eng.*
23. Zhu, Y.Y. and Cescotto, S. (1994) Transient thermal and thermomechanical analysis by FEM. *Computers and Structures*, **53**, 2, 275-304.
24. Zhu, Y.Y., Cescotto, S. (1995) Unified and mixed formulation of the 4-node quadrilateral elements by assumed strains method : application to thermomechanical problems. *Int. J. for Num. Meth. in Eng.*, **38**, 685-716.
25. Needleman, A., Tvergaard, V. (1984) An analysis of ductile rupture in notched bars, J. Mech. Phys. Solids, **32**, 461-490.